Exploiting Zone-Folding Induced Quasi-Bound Modes to Achieve Highly Coherent Thermal Emissions

Kaili Sun, Uriel Levy, and Zhanghua Han*

ACCESS | Metrics & More | Article Recommendations | Supporting Information

ABSTRACT: Thermal emissions with high coherence, although not as high as those of lasers, still play a crucial role in many practical applications. In this work, by exploiting the geometric perturbation-induced optical lattice tripling and the associated Brillion zone folding effect, we propose and investigate thermal emissions in the mid-infrared with simultaneous high temporal and spatial coherence. In contrast with the case of period-doubling perturbation in our previous work, the steeper part of the guided mode dispersion band will be folded to the high-symmetry Γ point in the ternary grating. In this case, a specific emission wavelength corresponds to only a very small range of wavevectors. Consequently, apart from the high temporal coherence characterized by an experimental bandwidth around 30 nm, the achieved thermal emissions also feature ultrahigh spatial coherence. Calculations show that at the thermal emission wavelengths in the mid-infrared, the spatial coherence length can easily reach up to mm scale.

KEYWORDS: ternary grating, Brillion zone-folding, quasi-guided mode, mid-infrared, coherent thermal emitters
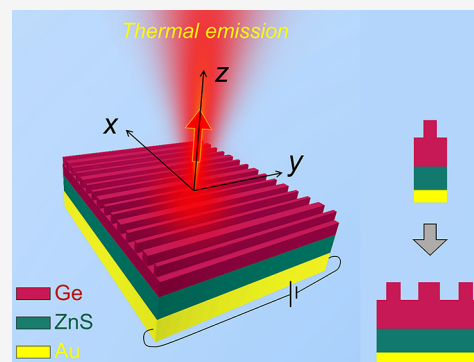
A conventional thermal emitter (TE) can be well-approximated by the concept of blackbody, and its thermally induced radiations are normally broadband and incoherent in the far-field. This is because the thermally excited charged particles generate randomly oriented dipoles with different momentums within the material, resulting in a typical behavior of the emissivity with a broad-spectral band and a quasi-isotropic angular distribution. After the periodic microstructure was first demonstrated to emit coherent and linearly polarized thermal radiations,[1] new doors have been opened for controlling the spectral, coherence, and polarization properties of thermal emissions.[2,3] In recent years, there has been increasing interest in developing micro/nanostructures to achieve coherent TEs, especially with spectral selectivity (temporal coherence) and directional control (spatial coherence) for applications in thermal photovoltaic systems,[4] infrared imaging,[5] gas sensing,[6] and radiative cooling.[7] Currently, researchers have been successful in this direction by employing various physics in different photonic structures. The key to realizing coherent TEs is to couple the broadband thermal fluctuations to some optical resonances, which will further direct the proper spectral component to free space. Examples of the optical resonances include delocalized optical surface waves like surface plasmon polaritons (SPPs) excited by plasmonic bandgap structures[8] or metallic gratings[9] and surface phonon polaritons (SPhPs) supported by polar materials with similar periodic textures.[10−13] Localized plasmonic resonances supported by the metal−insulator−metal (MIM) sandwich geometry[14,15] are also widely used, where the radiation resonance is generally determined by the top-layer metamaterial and the thickness of the central layer can be used to control the emissivity. However, large limitations exist for the previous approaches. For example, TEs based on SPhPs suffer from a limited working range known as the Reststrahlen band. Due to the high intrinsic loss of metals, the radiation spectrum of the MIM structure has a typical broad line width ($Q < 40$), implying poor temporal coherence. Coherent TEs based on the moiré effect in double-layer twisted gratings on a tungsten substrate have also been explored, but the complex structure geometry is difficult to implement in practice.[16]

In recent years, all-dielectric nanostructures have received widespread attention due to their extremely low absorption loss and unique optical properties to support high-quality (Q) factor resonances.[17] A commonly used design strategy for achieving such high-Q resonances is to start from some well-constrained bound modes (BMs). One typical example of the BM is the bound state in the continuum (BIC),[18,19] which has been intensively studied. The BIC usually occupies discrete points in the energy-momentum space and has an infinite Q factor (resonance line width is 0) due to the inability to couple with free space radiations. By introducing geometric
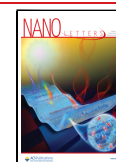
perturbations or tilted incidence conditions, BIC can be transformed into quasi-BIC (QBIC) to form high Q resonance modes,[20,21] which have narrow bandwidth. Another type of BMs, the guided modes (GMs), have broadband infinite Q factors, and its dispersion band can be folded into the continuum by introducing periodic perturbations to form quasi-GMs (QGMs).[22−24] Compared to QBIC, the QGMs have the Q factors inherently not sensitive to the wavevector/frequency, i.e., with robustness. The QGM inherits the steep dispersion of the original GM and thus have spectral tunability over the entire dispersion band while maintaining the high-Q characteristic.[22,25] This property enables good control over the spectral position by only varying the incident angle, with no negative influence to the Q. We note that both QBIC and QGM are collective behaviors in the periodic structures and require a large number of unit cells to achieve high Q values.[26] In order to achieve thermal radiation with good coherence, thermal fluctuations should couple to nonlocal resonances of periodic optical elements, allowing them to propagate over long distances before coupling to the external. In our previous studies, we tried to apply the above two concepts to thermal radiation sources and have obtained good experimental demonstrations.[27,28] However, achieving large spatial coherence of the thermal radiations in the normal direction still demands significant improvement. For the GM supported by a regular sub-wavelength photonic lattice, periodic modulation of the structure results in a coupling between two counter-propagating modes and gives rise to a spectral gap at the boundary of the first Brillouin zone (FBZ), featuring a local flat band within a certain range of wavevectors. When the lattice is distorted, e.g., doubled by some geometric perturbation, the spectral gap is usually folded to the Γ point. This will give rise to poor spatial coherence of radiation in the normal direction when the structure is employed as a TE. That is because these QGMs close to the Γ point have a large number of excited modes within a small Δk, and the thermal radiation emitted at that frequency will include many spatial/Fourier components. These components dephase on a length scale on the order of $1/\Delta k$, resulting in a low spatial coherence length. So in order to achieve a thermal emission with high spatial coherence, one should try to exploit the QGMs with a steep dispersion.

In this work, we change the width of every third ridge in a regular grating to enable the period-tripling of the lattice, which will cause the FBZ to shrink to 1/3 of its original. As a result, the dispersion curve of the infinite-Q GMs will be folded at the boundary of the new FBZ to be above the light line to form QGMs with ultrahigh Q factors.[22] As an example of a demonstration, such a ternary grating structure on a Ge slab waveguide is used and separated from a gold reflector by a low refractive index layer of ZnS. By heating the metal substrate with electric current, a reservoir of broadband thermal fluctuations can be provided, and the spectral component matching the nonlocal mode of QGM will couple to it and be extracted to free space in the form of coherent thermal emissions with enhanced efficiency due to the Purcell effect. Unlike the binary grating,[28] the spectral gap at the original FBZ boundary still appears at the boundary of the new FBZ in the ternary grating, while the steeper part of the dispersion curve of the original GMs (at 2/3 of the original FBZ) will emerge at the Γ point. In other words, when the TE operates in the normal direction, the emission occurs only within a very small range of wavevectors, resulting in a much narrower angular distribution and a larger coherence length.

Figure 1(a) schematically illustrates the working principle of the TE. A sufficiently thick region of gold is employed at the
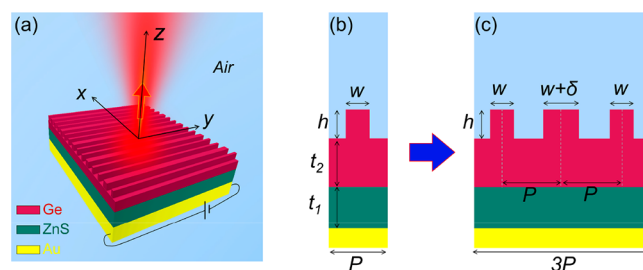
Figure 1. (a) Schematic diagram illustrates the working principle of the highly coherent TE. (b, c) The unit cells of the (b) regular and (c) ternary gratings after the introduction of the perturbation δ, respectively.

bottom to work as a conducting layer. To achieve nonlocal QGMs, a high-refractive index and low-loss Ge is used as both the top grating and waveguide core layer. ZnS is inserted in the middle as a low-refractive index buffer. Figure 1(b,c) depicts the evolution process from a regular grating to the ternary grating structure by introducing δ. Through careful design, the following set of geometric parameters are used: $P = 720$ nm, $t_1 = 880$ nm, $t_2 = 440$ nm, $h = 390$ nm, and $w = 220$ nm. The period P of the structure, the slab thickness, and the size of the ridges will determine the radiation wavelength of the QGMs, while the ridge width difference δ determines the radiation Q factor of the whole structure. The ZnS thickness t_1 of the buffer layer can be adjusted, and it has two additional roles. On one hand, it can control the impedance matching between the structure and the environment to optimize the emissivity. On the other hand, it isolates the core layer from the metal, reducing the impact of metal absorption on the optical modes (see the Supporting Information Part III for all material refractive index parameters in the calculations). According to Kirchhoff's law of thermal radiation, the emissivity for any object is equal to the absorptivity under thermodynamic equilibrium conditions. So, in the calculations, the absorbance of a structure $A(\omega)$ can be used to model the emissivity $E(\omega)$. Since the gold substrate is optically thick enough to result in zero transmittance, the emissivity $E(\omega) = A(\omega) = 1 - T(\omega) - R(\omega)$ can be simplified as $E(\omega) = A(\omega) = 1 - R(\omega)$. Therefore, it is only necessary to study the absorption characteristics of the structure, and the results will represent the emission properties of the structure. In practical applications, when an electric current is applied to the bottom metal layer to function as a Joule heater, the thermally excited charged particles generate randomly oriented dipoles in the material that couple to the QGMs supported by the upper structure. Ultimately, the coherent light is radiated with an enhanced efficiency.

In general, for the transformation from GM into QGM, geometric perturbation is required to increase the period P in a sub-wavelength lattice to the new period $P_m = mP$, where m is an integer representing the number of periods from the original structure that must be merged into the new unit. Band folding typically occurs at the boundary of the new FBZ, i.e., at wavevectors of $\pm\pi/P_m$. Due to the periodicity in the wavevector space, the original dispersions at $\pm 2\pi/P_m$ are folded to the Γ point. In previous studies, researchers have used period-doubling to enhance the angular tolerance of
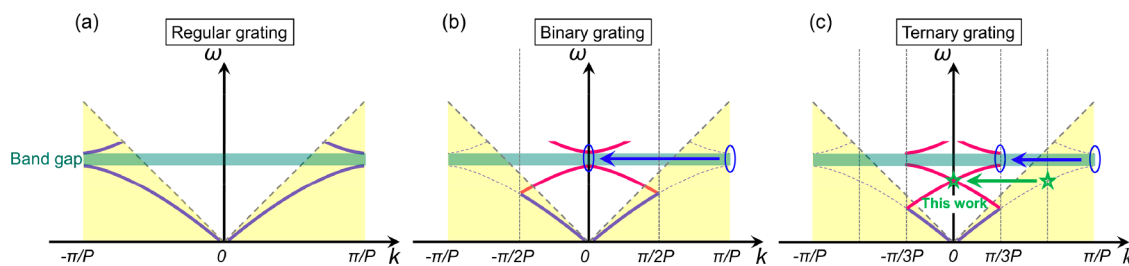
Figure 2. Schematic diagram of dispersion variation supported by (a) regular gratings with a period of P, (b) binary gratings with the period perturbed to $2P$, and (c) ternary gratings with the period perturbed to $3P$.

devices,[29] taking advantage of the larger spectral bandgap at the boundary of the FBZ of a regular grating. To illustrate the evolution from GM to QGM involved in this study, we start with a regular grating with a sub-wavelength period P, the cross section of which is schematically shown in Figure 1(b). For such a grating, the coupling between two counterpropagating modes leads to a pronounced spectral gap at the boundary of the FBZ ($k = \pm\pi/P$), and close to this position, the group velocity decreases. Furthermore, the magnitude of the refractive index modulation by the grating determines the broadness of the spectral gap. When a perturbation is introduced, e.g., by changing the width or position of every second ridge, the period changes from P to $2P$ resulting in band folding at the position of $k = \pm\pi/2P$, as shown in Figure 2(b). The blue circle indicates that the original spectral gap is folded to the Γ point, which results in the thermal emission appearing within a wider range of wavevectors, thereby reducing its spatial coherence. While low-contrast gratings can be used to reduce the size of the spectral gap,[30] the suppressed radiation losses in lossy systems will be harmful to achieve a large emissivity due to the absence of Q matching. For the ternary gratings in Figure 1(c), due to the increase of the period from P to $3P$, the FBZ shrinks to $[-\pi/3P, \pi/3P]$ in the wavevector space, as shown in Figure 2(c). The spectral gap at the boundary of the FBZ of regular grating $k = \pm\pi/P$ is moved to the new boundary of the FBZ, and the continuous GM band originally located at $k = \pm2\pi/3P$ is folded to the Γ point. As indicated by the green pentagram in Figure 2(c), a state similar to degeneracy is formed at the Γ point, which ensures that the emission at the Γ point occurs only in the very small interval Δk.

We computed the band diagrams of the GM/QGM modes supported by both the regular grating and the ternary grating where δ is assumed to be 50 nm. All the calculations are carried out using the finite element method (FEM) implemented in the commercial software COMSOL Multiphysics. In Figure 3(a), the yellow region represents the area below the light line, where the modes have infinite Q factors. The blue arrow illustrates the effect of the band folding in the case of the period tripling. Since $m = 3$, the continuous GM at the position of $2\pi/3P$ in the regular grating appears at the Γ point, as shown by the transition from the blue dashed line circle to the blue solid line circle in the figure. In this work, we only focus on the two lowest-order bands A and B. Due to the weak coupling between two counterpropagating modes at $k = 0$, a spectral gap is present at the Γ point, which is much smaller than the period-doubling case in Figure 2(b). Such a tiny spectral gap is necessary for achieving high spatial coherence. Figure 3(b) presents a two-dimensional (2D) mapping of the emissivity across the entire FBZ for the ternary grating structure, and the inset shows a close-up at the intersection of
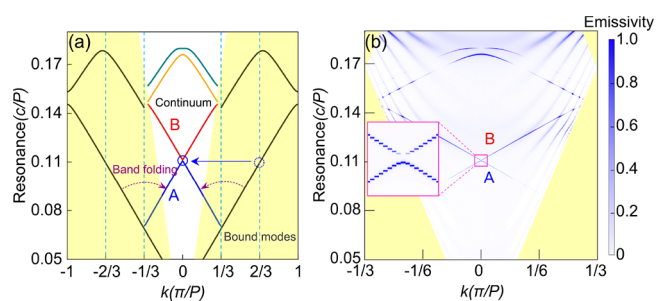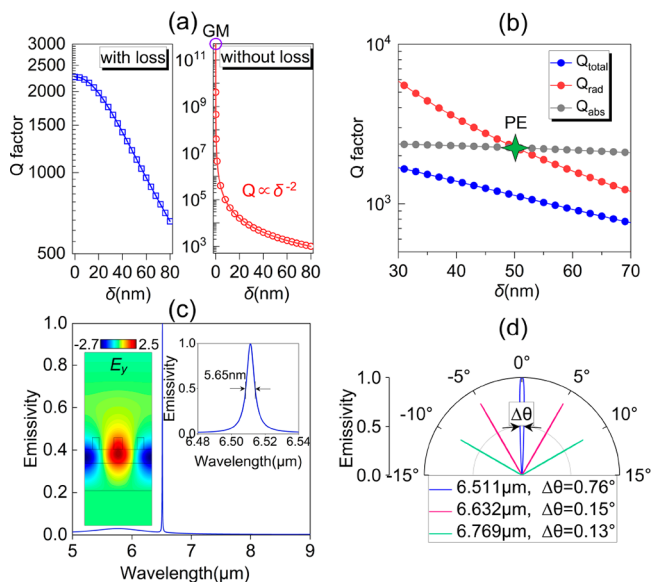

Figure 3. (a) The calculated band structures of the GM by the regular grating (solid black lines) and the QGM by the ternary grating (solid colored lines) with $\delta = 50$ nm. Only the wavevector along the k_x direction is considered. (b) 2D mapping of the emission spectrum within the FBZ using the ternary grating. (inset) A close-up of the spectral gap at the Γ point.

the two bands. The results agree quite well with those from the eigenfrequency analysis in Figure 3(a), with band-A and band-B exhibiting narrowband resonant spectra showing high robustness against wavevectors. The band-B shows a BIC at the Γ point, which arises from the structure's mirror-symmetry with respect to the center of the perturbed grating ridge. This symmetry-protected or fully antisymmetric mode cannot be excited by plane waves or radiate into free space. So we only consider the contribution of band-A. In fact, in the normal output direction of the TE, only an extremely narrow QGM resonance peak is present throughout the frequency range of $0.05c/P - 0.17c/P$, demonstrating its excellent monochromatic performance. Changing the position of some ridges without affecting their widths is another way of achieving the period tripling.[22,31] However, such a ternary grating with a positional perturbation will result in the entire system with no mirror symmetry. So both bands will radiate toward free space at the Γ point, and the monochromaticity of emissions in the normal direction will no longer be maintained.

The temporal coherence of a thermal emitter is primarily determined by the total Q factor (Q_{total}), which has two contributions $1/Q_{total} = 1/Q_{rad} + 1/Q_{abs}$ where the radiation Q factor (Q_{rad}) and absorption Q factor (Q_{abs}) are due to radiation loss and material absorption loss,[32] respectively. Therefore, the achievement of a high Q factor requires simultaneously high Q_{rad} and Q_{abs}. To simplify our experiments, all materials were deposited by electron beam evaporation (EBE), giving rise to their amorphous states. By adjusting the size of the δ to control the radiation loss, a total Q factor of more than 2×10^3 can still be achieved even when all the losses are considered. In fact, when all the materials except metals are single-crystalline and lossless, the Q factor can reach the order of 10^4 (see Figure S6). To illustrate the
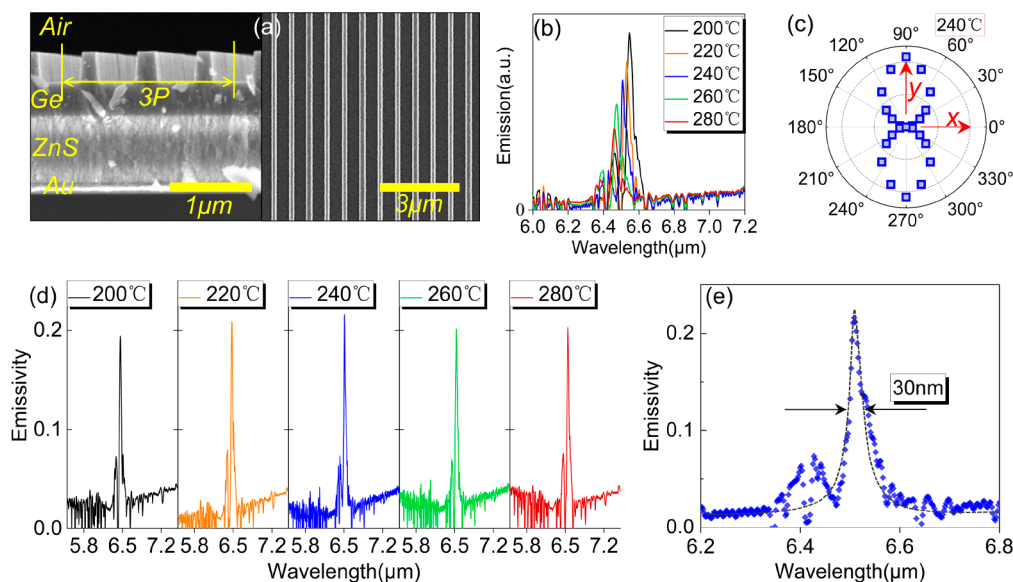
underlying physics, we consider the bottom metal as a perfect electric conductor (PEC) and neglect the losses in all other materials. In this case, the relationship between the Q factor and δ is shown on the right panel of Figure 4(a). As δ

increases, the Q factor exhibits an inverse quadratic dependence on δ. When δ = 0 nm, the dispersion of QGM restores to that below the light line, forming a GM with an infinite Q factor. As shown in Figure 4(b), when δ = 50 nm, $Q_{rad} = Q_{abs}$. According to the temporal coupled mode theory (TCMT), perfect emission (PE) is then achieved. The reflectivity spectra from the structure at different values of δ can be found in the Supporting Information (Figure S7), which are consistent with the results here. The corresponding emission spectrum exhibits excellent monochromaticity over a wide spectral range (5−9 μm), as shown in Figure 4(c), and exhibits an output line width of only 5.65 nm at 6.511 μm even when all the material losses are taken into account. Compared with traditional TEs based on MIM or SPhPs, the line width is reduced by 2 orders of magnitude. The inset on the left shows the field distribution of the real part of E_y at the emission peak wavelength, which is mainly concentrated in the high refractive index waveguide layer below each ridge. Figure 4(d) shows the spatial angular distribution of the emissivity for three different output wavelengths. At 6.511 μm, which corresponds to the normally emitted thermal radiation from the structure surface, the full width at half-maximum (fwhm) of the angular distribution is only 0.76° (13.26 mrad), indicating that the spatial coherence length[1] for the normal output emission is as high as $L_c = \lambda/\Delta\theta$ = 75.5λ = 0.491 mm. This represents an increase by more than 4 times compared to that of the thermal emission in the normal direction from a binary grating (L_c = 0.121 mm).[28] In addition, for a longer output wavelength of 6.769 μm in the inclined output direction, the spatial coherence length reaches L_c = 2.98 mm. Further results (see Figure S8) show that if lower contrast gratings made of single-crystal materials are used, the coherence length of the normal output emission can reach up to L_c = 1910λ = 13.27 mm.

In the experiment, we fabricated the above designed structure (the details can be found in the Supporting Information). The cross-sectional and top-view scanning electron microscope (SEM) images are shown in Figure

Figure 4. (a) Dependence of the Q factor on perturbation parameter δ. The blue curve gives the results using evaporated amorphous materials, while the red curve corresponds to the results where the losses of all materials are neglected. (b) Dependence of Q_{total}, Q_{abs}, and Q_{rad} on δ. When δ = 50 nm, $Q_{abs} = Q_{rad}$, perfect emission (PE) is achieved. (c) Normalized emission spectrum from the structure in the normal direction and at y-polarization. (inset, right) An enlarged view of the emission peak. (inset, left) The field distribution of the real part of E_y in the x-z plane at the peak wavelength. (d) The angular distribution of the emissivity at different emission wavelengths and output directions.

Figure 5. (a) Cross-sectional and top views of the fabricated structure obtained with SEM. (b) Emission spectrum of the fabricated sample at different temperatures (200, 220, 240, 260, and 280 °C) under y-polarization. (c) The polarization dependence of the peak emission intensity at 240 °C. (d) Normalized emission spectra at five different temperatures (normalized to a blackbody heated to the same temperature). (e) An enlarged view of the normalized emission spectrum at 240 °C, where the black dashed line represents a Lorentz fitting of the resonance.

5(a). The entire sample was heated to high temperatures using a commercial emission adapter, and the thermal radiation was characterized using a Fourier transform infrared (FTIR) spectrometer equipped with a linear polarizer (Figure S2). The *y*-polarized emission spectrum is shown in Figure 5(b), where the emission intensity exhibits an increase at higher temperatures, accompanied by a slight red-shift in the spectrum which is attributed to the thermo-optic effect of the Ge material. This indicates that the temperature can serve as a means of fine spectral tuning (Figures S5 and S9). The polarization dependence of the TE output was verified by rotating the direction of the polarizer at 240 °C, as shown in Figure 5(c). The normalized spectra at five different temperatures are shown in Figure 5(d), all normalized to blackbody radiation at the same temperature. It can be observed that a remarkably narrow emission spectrum is obtained over a wide wavelength range. The Q factor is generally stable and undergoes very slight changes with increasing temperature (see the results in Figure S9). Figure 5(e) shows an enlarged view at the wavelength peak position of 6.509 μm at 240 °C. An emission line width of only 30 nm is found, corresponding to a Q factor of 217. The experimental bandwidth is slightly lower than the theoretical predictions, mainly attributed to a lower Q_{abs} in the fabricated structure, resulting from the additional scattering losses introduced by the roughness of the structure sidewalls. The reduced emissivity from unity is attributed to a subsequent mismatch between Q_{abs} and Q_{rad}. Furthermore, all the thermal radiations exhibit good spatial coherence, even though multiple wavelengths in different radiation directions may simultaneously enter the FTIR and lead to the broadening of the emission line width.

It should be emphasized that in order to simplify the experiments, all of the thin films were obtained through evaporations, which results in higher absorption losses. If single-crystalline thin films are obtained by using more advanced techniques such as atomic layer deposition or molecular beam epitaxy in practical applications, combining with an optimization of the δ value to achieve a high emissivity, the Q factor can be increased to the order of 10^4 (see Figures S6 and S8). Additionally, this thermal emitter exhibits high spatial coherence due to the steep dispersion of the QGMs. In other words, the emitted wavelength is highly sensitive to the output angle with different angles corresponding to different output wavelengths. Since our measurement setup collects all of the emissions entering its entrance window within a certain range of angles, it leads to a spectral overlap and increases the spectral bandwidth. For a thermal radiation source in practical applications, a spatial filter can be combined to customize the radiation in a specific directional angle, then the emitter can achieve both ultranarrow line widths and high tuning of the output wavelength within a wide band (see Figure S7).

In summary, we achieved a high Q factor QGM with a small spectral gap and a less-rounded dispersion near the Γ point by utilizing the band folding effect in a ternary grating. The feasibility of its application in thermal emitters has been numerically investigated and has been experimentally demonstrated. Due to the period increase from P to $3P$, the large spectral gap at the original FBZ boundary is shifted to the boundary of the new FBZ, rather than being folded to the Γ point like that in a binary grating. The steep dispersion band of the GM at 2/3 of the original FBZ appears at the Γ point. Thanks to the small spectral gap and steeper dispersion combined with the high Q factor, thermal emissions of both

high temporal and high spatial coherence in the normal direction can be achieved. Furthermore, this thermal emitter offers a large spectral tunability by the output angle and linear polarization characteristics. This structurally simple and high-performance thermal radiation source represents the latest technological advancement in the field and is expected to become a promising alternative mid-infrared light source in applications such as the next-generation nondispersive infrared (NDIR) sensing systems.

■ ASSOCIATED CONTENT

Ⓢ Supporting Information

The Supporting Information is available free of charge at https://pubs.acs.org/doi/10.1021/acs.nanolett.3c04587.

> Details of the device fabrication process; more information on the optical measurement setup; Material parameters for the simulations, and some further simulation results on the thermal emission properties (PDF)

■ AUTHOR INFORMATION

Corresponding Author

Zhanghua Han — *Shandong Provincial Key Laboratory of Optics and Photonic Devices, Center of Light Manipulation and Applications, School of Physics and Electronics, Shandong Normal University, Jinan 250358, China;* ⓞ orcid.org/0000-0002-4177-2555; Email: zhan@sdnu.edu.cn

Authors

Kaili Sun — *Shandong Provincial Key Laboratory of Optics and Photonic Devices, Center of Light Manipulation and Applications, School of Physics and Electronics, Shandong Normal University, Jinan 250358, China;* ⓞ orcid.org/0000-0002-4455-5177

Uriel Levy — *Department of Applied Physics, Hebrew University of Jerusalem, Jerusalem 91904, Israel;* ⓞ orcid.org/0000-0002-5918-1876

Complete contact information is available at:
https://pubs.acs.org/10.1021/acs.nanolett.3c04587

Notes

The authors declare no competing financial interest.

■ ACKNOWLEDGMENTS

■ REFERENCES

(1) Greffet, J.-J.; Carminati, R.; Joulain, K.; Mulet, J.-P.; Mainguy, S.; Chen, Y. Coherent Emission of Light by Thermal Sources. *Nature* **2002**, *416*, 61−64.

(2) Baranov, D. G.; Xiao, Y.; Nechepurenko, I. A.; Krasnok, A.; Alù, A.; Kats, M. A. Nanophotonic Engineering of Far-Field Thermal Emitters. *Nat. Mater.* **2019**, *18* (9), 920−930.

(3) Chae, H. U.; Shrewsbury, B.; Ahsan, R.; Ghanekar, A.; Povinelli, M. L.; Kapadia, R. Monolithic III-V on Metal for Thermal Metasurfaces. *ACS Nano* **2022**, *16* (11), 18497−18502.

(4) Rephaeli, E.; Fan, S. Absorber and Emitter for Solar Thermo-Photovoltaic Systems to Achieve Efficiency Exceeding the Shockley-Queisser Limit. *Opt. Express* **2009**, *17* (17), 15145.

(5) Hermes, M.; Morrish, R. B.; Huot, L.; Meng, L.; Junaid, S.; Tomko, J.; Lloyd, G. R.; Masselink, W. T.; Tidemand-Lichtenberg, P.;

Pedersen, C.; et al. Mid-IR Hyperspectral Imaging for Label-Free Histopathology and Cytology. *J. Opt. (United Kingdom)* **2018**, *20* (2), 023002.

(6) Gong, Y.; Wang, Z.; Li, K.; Uggalla, L.; Huang, J.; Copner, N.; Zhou, Y.; Qiao, D.; Zhu, J. Highly Efficient and Broadband Mid-Infrared Metamaterial Thermal Emitter for Optical Gas Sensing. *Opt. Lett.* **2017**, *42* (21), 4537.

(7) Raman, A. P.; Anoma, M. A.; Zhu, L.; Rephaeli, E.; Fan, S. Passive Radiative Cooling below Ambient Air Temperature under Direct Sunlight. *Nature* **2014**, *515* (7528), 540−544.

(8) Biener, G.; Dahan, N.; Niv, A.; Kleiner, V.; Hasman, E. Highly Coherent Thermal Emission Obtained by Plasmonic Bandgap Structures. *Appl. Phys. Lett.* **2008**, *92*, 081913.

(9) Laroche, M.; Arnold, C.; Marquier, F.; Carminati, R.; Greffet, J.-J.; Collin, S.; Bardou, N.; Pelouard, J.-L. Highly Directional Radiation Generated by a Tungsten Thermal Source. *Opt. Lett.* **2005**, *30* (19), 2623.

(10) Dahan, N.; Niv, A.; Biener, G.; Gorodetski, Y.; Kleiner, V.; Hasman, E. Enhanced Coherency of Thermal Emission: Beyond the Limitation Imposed by Delocalized Surface Waves. *Phys. Rev. B* **2007**, *76* (4), 045427.

(11) Arnold, C.; Marquier, F.; Garin, M.; Pardo, F.; Collin, S.; Bardou, N.; Pelouard, J.-L.; Greffet, J.-J. Coherent Thermal Infrared Emission by Two-Dimensional Silicon Carbide Gratings. *Phys. Rev. B* **2012**, *86* (3), 035316.

(12) Ma, B.; Huang, Y.; Zha, W.; Qin, B.; Qin, R.; Ghosh, P.; Kaur, S.; Qiu, M.; Li, Q. Narrowband Diffuse Thermal Emitter Based on Surface Phonon Polaritons. *Nanophotonics* **2022**, *11* (17), 4115−4122.

(13) Lu, G.; Gubbin, C. R.; Nolen, J. R.; Folland, T.; Tadjer, M. J.; de Liberato, S.; Caldwell, J. D. Engineering the Spectral and Spatial Dispersion of Thermal Emission via Polariton-Phonon Strong Coupling. *Nano Lett.* **2021**, *21* (4), 1831−1838.

(14) Liu, X.; Tyler, T.; Starr, T.; Starr, A. F.; Jokerst, N. M.; Padilla, W. J. Taming the Blackbody with Infrared Metamaterials as Selective Thermal Emitters. *Phys. Rev. Lett.* **2011**, *107* (4), 045901.

(15) Lochbaum, A.; Fedoryshyn, Y.; Dorodnyy, A.; Koch, U.; Hafner, C.; Leuthold, J. On-Chip Narrowband Thermal Emitter for Mid-IR Optical Gas Sensing. *ACS Photonics* **2017**, *4* (6), 1371−1380.

(16) Guo, C.; Guo, Y.; Lou, B.; Fan, S. Wide Wavelength-Tunable Narrow-Band Thermal Radiation from Moiré Patterns. *Appl. Phys. Lett.* **2021**, *118* (13), 131111.

(17) Huang, L.; Xu, L.; Powell, D. A.; Padilla, W. J.; Miroshnichenko, A. E. Resonant Leaky Modes in All-Dielectric Metasystems: Fundamentals and Applications. *Phys. Rep.* **2023**, *1008*, 1−66.

(18) Hsu, C. W.; Zhen, B.; Stone, A. D.; Joannopoulos, J. D.; Soljačić, M. Bound States in the Continuum. *Nat. Rev. Mater.* **2016**, *1* (9), 16048.

(19) Wang, J.; Kühne, J.; Karamanos, T.; Rockstuhl, C.; Maier, S. A.; Tittl, A. All-Dielectric Crescent Metasurface Sensor Driven by Bound States in the Continuum. *Adv. Funct. Mater.* **2021**, *31* (46), 1−10.

(20) Koshelev, K.; Lepeshov, S.; Liu, M.; Bogdanov, A.; Kivshar, Y. Asymmetric Metasurfaces with High- Q Resonances Governed by Bound States in the Continuum. *Phys. Rev. Lett.* **2018**, *121* (19), 193903.

(21) Azzam, S. I.; Shalaev, V. M.; Boltasseva, A.; Kildishev, A. V. Formation of Bound States in the Continuum in Hybrid Plasmonic-Photonic Systems. *Phys. Rev. Lett.* **2018**, *121* (25), 253901.

(22) Sun, K.; Wei, H.; Chen, W.; Chen, Y.; Cai, Y.; Qiu, C.-W.; Han, Z. Infinite-Q Guided Modes Radiate in the Continuum. *Phys. Rev. B* **2023**, *107*, 115415.

(23) Overvig, A. C.; Shrestha, S.; Yu, N. Dimerized High Contrast Gratings. *Nanophotonics* **2018**, *7* (6), 1157−1168.

(24) Wang, W.; Srivastava, Y. K.; Tan, T. C.; Wang, Z.; Singh, R. Brillouin Zone Folding Driven Bound States in the Continuum. *Nat. Commun.* **2023**, *14* (1), 2811.

(25) Sun, K.; Cai, Y.; Levy, U.; Han, Z. Quasi-Guided Modes Resulting from the Band Folding Effect in a Photonic Crystal Slab for Enhanced Interactions of Matters with Free-Space Radiations. *Beilstein J. Nanotechnol.* **2023**, *14*, 322−328.

(26) Overvig, A.; Alù, A. Diffractive Nonlocal Metasurfaces. *Laser Photonics Rev.* **2022**, *16* (8), 202100633.

(27) Sun, K.; Sun, M.; Ma, Y.; Shi, Y.; Han, Z. Ultra-Narrow Bandwidth Mid-Infrared Thermal Emitters Achieved with All-Dielectric Metasurfaces. *Int. Commun. Heat Mass Transfer* **2023**, *143*, 106728.

(28) Sun, K.; Levy, U.; Han, Z. Thermal Emission with High Temporal and Spatial Coherence by Harnessing Quasiguided Modes. *Phys. Rev. Appl.* **2023**, *20* (2), 024033.

(29) Lemarchand, F.; Sentenac, A.; Giovannini, H. Increasing the Angular Tolerance of Resonant Grating Filters with Doubly Periodic Structures. *Opt. Lett.* **1998**, *23* (15), 1149.

(30) Huang, L.; Jin, R.; Zhou, C.; Li, G.; Xu, L.; Overvig, A.; Deng, F.; Chen, X.; Lu, W.; Alù, A.; et al. Ultrahigh-Q Guided Mode Resonances in an All-Dielectric Metasurface. *Nat. Commun.* **2023**, *14* (1), 3433.

(31) Jin, R.; Huang, L.; Zhou, C.; Guo, J.; Fu, Z.; Chen, J.; Wang, J.; Li, X.; Yu, F.; Chen, J.; et al. Toroidal Dipole BIC-Driven Highly Robust Perfect Absorption with a Graphene-Loaded Metasurface. *Nano Lett.* **2023**, *23* (19), 9105−9113.

(32) Seok, T. J.; Jamshidi, A.; Kim, M.; Dhuey, S.; Lakhani, A.; Choo, H.; Schuck, P. J.; Cabrini, S.; Schwartzberg, A. M.; Bokor, J.; et al. Radiation Engineering of Optical Antennas for Maximum Field Enhancement. *Nano Lett.* **2011**, *11* (7), 2606−2610.